Article

Investigation of the Time-Lapse Changes with the DAS Borehole Data at the Brady Geothermal Field Using Deconvolution Interferometry

Hilary Chang [1,†,*] **and Nori Nakata** [1,2,†]

[1] Massachusetts Institute of Technology, 77 Massachusetts Avenue, 54-216, Cambridge, MA, 02139, USA; nnakata@mit.edu,
[2] Lawrence Berkeley National Laboratory, CA 94720, USA

* Correspondence: hilarych@mit.edu

† These authors contributed equally to this work.

Abstract: The distributed acoustic sensing (DAS) has great potential for monitoring natural-resource reservoirs as well as borehole conditions. However, the large volume of data, complicated wavefield, and higher noise level often make processing and interpretation difficult. To this end, seismic interferometry based on deconvolution becomes a convenient tool for analyzing complex wavefield and extracting coherent waves from noise. It separates the structure response and allows us to examine the wavefields that satisfy different boundary conditions. Thus, we can utilize the dense spatial coverage of DAS receivers deployed in the borehole for monitoring structural changes, diagnosing well-casing integrity, and constrain the seismic energy sources in space and time. We apply this technique on the DAS data in the vertical borehole at the Brady geothermal field in Nevada to extract coherent and interpretable waves. Using results from analytical and numerical modeling, we discover that a simple string model can explain the extracted coherent waves well. By analyzing the strong reverberating signals due to resonance of the upper borehole casing with this numerical model, we constrain the dominant energy sources in the system and the configuration of the structure that causes the resonance. We investigate the propagating velocity of the extracted waves as well as the velocity variation with depth, observation time, temperature, and pressure. The velocity variations due to these parameters suggest that the waves are sensitive to thermal condition, casing condition, and borehole processes induced by pressure changes. The amplitude spectra of the deconvolved wavefields show clear normal modes of such reverberations, which are useful for dispersion analysis of the waves. At the bottom half of the borehole, which does not show clear resonance, we only obtain signals during the active seismic operation time due to poor coupling. To extract the time-lapse changes of formation, we need better coupling between DAS cables and the borehole.

Keywords: distributed acoustic sensing; borehole; time-lapse

Citation: Chang, H.; Nakata, N. Time-lapse changes with the DAS borehole data using deconvolution interferometry. *Preprints* **2021**, *1*, 0. https://doi.org/

Received:
Accepted:
Published:

1. Introduction

The distributed acoustic sensing (DAS) and distributed temperature sensing (DTS) have large potentials for applications in borehole environments, especially for geothermal reservoir monitoring. Applications of DAS in boreholes include flow monitoring [1–3], wellbore diagnostics [1,3,4], time-lapse structural monitoring with vertical seismic profiling [5–8], micro-seismicity detection [9], and long-period long-duration event detection

for monitoring the response of hydraulic fracture [10]. Especially, DAS is suitable for geothermal reservoir monitoring for several reasons [11,12]: First, the DAS fiber has higher endurance in high temperature, high pressure, and corrosive environments compared to geophones. Second, it provides a dense 1D receiver arrays along the wellbore. Finally, the cost of DAS borehole deployment is relatively low, although the interrogator and the data storage can be expensive. Once installed, the fiber can be left in the well for long-term monitoring without changing locations, which is one of the main difficulties for conventional 4D (3D and time) surveys. However, the primary challenge of DAS is its lower signal-to-noise ratio (SNR), and that good coupling is not trivial [9,13,14]. Furthermore, the wavefields in the borehole environment can also be complicated because of the superposition of many waves, which adds complications to time-lapse monitoring. In this study, we use seismic interferometry to extract signals from complex wavefields. The coherent wavefields we obtain can be used for monitoring the changes in the structure and diagnosing well-casing integrity, which is important for reducing greenhouse leaks during production.

We investigate the DAS data in a vertical borehole (DASV) from the PoroTomo project at the Brady geothermal field in Nevada [15,16]. The PoroTomo project was a four-week experiment conducted during March 2016, during which the team conducted vibroseis experiments under varying pumping operations and collected a variety of geophysical data including surface DAS (DASH), DASV, nodal geophones, InSAR, GPS, pressure, and temperature (DTS) data. The DASV data was only available in the last two weeks due to installation challenges [16]. Previous studies have analyzed the borehole DASV data and identified features related to changes of operations intensities [17–19]. Patterson *et al.* [17] and Patterson [18] analyzed the borehole DTS and pressure data to characterize the reservoir response at different stages of operations. Miller *et al.* [19] investigated the DASV data to find the signatures of earthquakes, vibroseis sweeps, and responses to the repetitive borehole processes. Trainor-Guitton *et al.* [20] migrated active seismic data observed at DASV between 160 - 300 m depth and successfully imaged features on two nearby steeply dipping faults ($\sim$1 km away). These studies suggest that the DASV data contains various signals at different portion of the cable. Some of these signals are reoccurring, such the vibration of the well-casing; some are transient, for example, the earthquakes and the vibroseismic active sources. What makes the data more complicated is the unknown coupling between the cable and the well-casing. The DASV cable is coupled to the wall of the borehole only through friction, which is enough for deviated wells [11] but might not provide sufficient SNR for the vertical well in Brady, especially when the temperature and pressure are rapidly changing. Poor coupling is also suggested by occasional cable slipping events observed in the data [19]. Our goal, therefore, is to extract useful and interpretable signals from these complex wavefields for time-lapse monitoring.

We use deconvolution seismic interferometry to extract coherent signals along the 1D receivers of the borehole DAS array. The coherent signals in the deconvolved wavefields are governed by the same wave physics (i.e., wave equation) [21]. Furthermore, the deconvolution modifies the boundary condition at the receiver used for deconvolution (i.e., the virtual source) [21–23]. This allows us to isolate the pure response of the structure from the influence of the boundary conditions. Hence, we can estimate seismic wave propagating velocities and the velocity variations of the system itself over time using these coherent signals. In addition, we can examine the waves in the deconvolved wavefields at different boundary conditions to constrain the energy sources [23]. Previous research using this deconvolution method include monitoring near-surface velocity changes in various time scales [24–27], analyzing the vibration modes of a building during earthquakes [23,28] and from ambient noise [29]. Here, we demonstrate this technique is a convenient tool for monitoring well-casing integrity. With this technique, we can deal with the large amount of DAS data and utilize the dense spatial coverage that DAS provides.

The structure of this study is as follows: We first introduce the Brady DASV data (Section 2), the deconvolution seismic interferometry method, and the coherent signals extracted from the data using the method (Section 3.1). This coherent signal we extract in the upper part of the borehole is mostly caused by the ringing of the borehole well-casing as suggested by Miller *et al.* [19]. We analyze and simulate this wavefield using 1D string models. We use this signal to monitor the velocity changes in the well-casing in the time domain (Section 3.2), and a normal-mode analysis for the vibration modes in the frequency domain (Section 3.3). In Section 4.1, we discuss the processes these waves are suspected to and the constrains that the analysis results put on the structure and energy sources. We discuss the transient signals we obtain in the lower part of the borehole in Section 4.2 and Appendix A.

2. Data

We focus on the DASV, the DTS temperature, and the pressure data from the PoroTomo project [15,16]. The DASV and DTS fibers are co-located in one borehole (red star in Figure 1; well 56-1) and the pressure sensor is located at a nearby well (green cross in Figure 1; well 56A-1). The DASV and DTS cables are nearly 380 m long in the well. The ground is about 1230 m above sea level near well 56-1 and 56A-1. In well 56-1, the inner (production) casing starts from the surface and down to 310 m. In the upper 0 - 87 m of well 56-1, an outer surface casing with a larger diameter is behind the inner production casing. The DASV system has 384 channels (i.e., receivers) with approximately 1 m channel spacing. The DASV fiber is single-mode and the DTS fibre is multi-mode, both are high temperature acrylate-coated, which is tested to be resilient up to 150°C. The cable is protected by 316 stainless steel double tubing. The DASV system has a gauge length of 10 m with sampling rate of 1000/s. Since DAS measures the average optical phase change across the gauge length, the unit of the observed data is radian/millisecond/gauge length. The total DASV data size is 981 GB stored in SEG-Y format. The DTS system has channel interval of 0.126 m and sampling interval of 62 s. The pressure sensor is at an elevation corresponding to channel 219 of the DASV system (i.e. measured depth = 219 m). The sampling interval of the pressure sensor is 60 s. The two wells are around 100 m away from each other; they were hydraulically connected as suggested by Patterson [18] based on simultaneous responses between the DTS and the pressure sensor.

The pressure and temperature profiles evolve in time, while the DASV data also show disturbances across space and time. The measurements of DASV, DTS, and pressure were continuous in time and overlapped for about eight days from 3/18 to the end of 3/25 in 2016 (Figure 2). The pressure was observed for a longer time. The analysis period starts with a drastic pressure drop during 3/18 due to increased operation after a long shutdown period. Then, the pressure increases slowly due to increasing injection until resuming to normal operation on 3/24. The pressure bump at the end of 3/25 is due to an unplanned plant shutdown [30]. The temperature profile in general increases with depth but is characterized by a heat deficit below 320 m due to historical geothermal explorations in this region [19]. The temperature was lower initially in early 3/18 because the well was cooled with water before cable installation for safety reasons. The temperature raised back slowly with time and reached its high of around 160°C at the depth of ∼260 m. The maximum temperature is around 160 °C.

We note some features in Figure 2 in below that are related to later interpretations. The first is the large disturbances caused by the depressurization processes. On 3/18 - 3/19, the depressurization processes following the pressure drop caused the steam/water interface to move downward from 115 to 120 m, as suggested by Patterson *et al.* [17] and Miller *et al.* [19] based on the trend of the temperature transitions (Figure 2b). During this time, the DC levels in the upper part of DASV were high (Figure 2c). Second, the casing structure

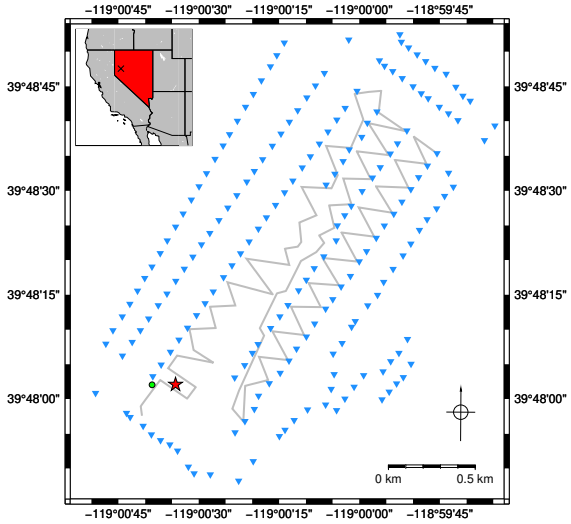

Figure 1. Configuration of the PoroTomo experiment. The survey was at the Brady geothermal field in Nevada, USA (black cross in the inset). The red star is the borehole (well 56-1) with DASV and DTS. The green dot is the borehole (well 56A-1) with the pressure sensor. The blue triangles are the locations of the vibroseis shots. The grey lines are the DASH cable on the surface. We use DASV, DTS, and pressure data in this study.

and fluid exchanges affect the data. Patterson *et al.* [17] observed advection possibly due to fluid movement at 165 m, where the casing might have a problem such as cracks or poor cement bonding. Below 310 m is the uncased zone with high permeability and provides a pathway for fluid [17]. These spots are potential locations for fluid to enter or exit the borehole from below in response to pressure changes. Third, the high RMS amplitudes at 90 m and below 350 m in Figure 2d were due to potential cement losing behind the casing and fluid exchange activities, respectively [19]. The higher DC values at these two spots show the slow strains induced by thermal effect [19]. Fourth, the surface diurnal cycles in Figure 2b - d are related to daily variations of noise level including exploration activities, and temperature.

3. Methods and analysis results

3.1. Extraction of coherent waves

3.1.1. Review of deconvolution interferometry

We use seismic interferometry by deconvolution to extract coherent wavefields from the data. The deconvolution method modifies the boundary conditions of the wavefield depending on the receiver used for deconvolution (i.e., the virtual source), which makes it suitable for obtaining the pure response of the structure [21]. Snieder and Safak [28] and Nakata *et al.* [23] took advantage of this property to separate the effect of ground coupling from the building response during earthquakes and extract the vibration modes of the building using receivers on the building floors. Thus, the deconvolution method is beneficial for time-lapse monitoring since the boundary conditions might change in time. Nakata and Snieder [26] monitored monthly and annually shear wave velocity changes at the near-surface by deconvolving surface and borehole sensors. Sawazaki *et al.* [24], Yamada *et al.* [25], and Bonilla *et al.* [27] used it to analyze the near-surface velocity changes during earthquake strong ground motions. Here, we use deconvolution seismic interferometry to isolate the response of the structure from the the unknown boundary condition at depth, which allows to perform time-lapse velocity tracking. In addition, we

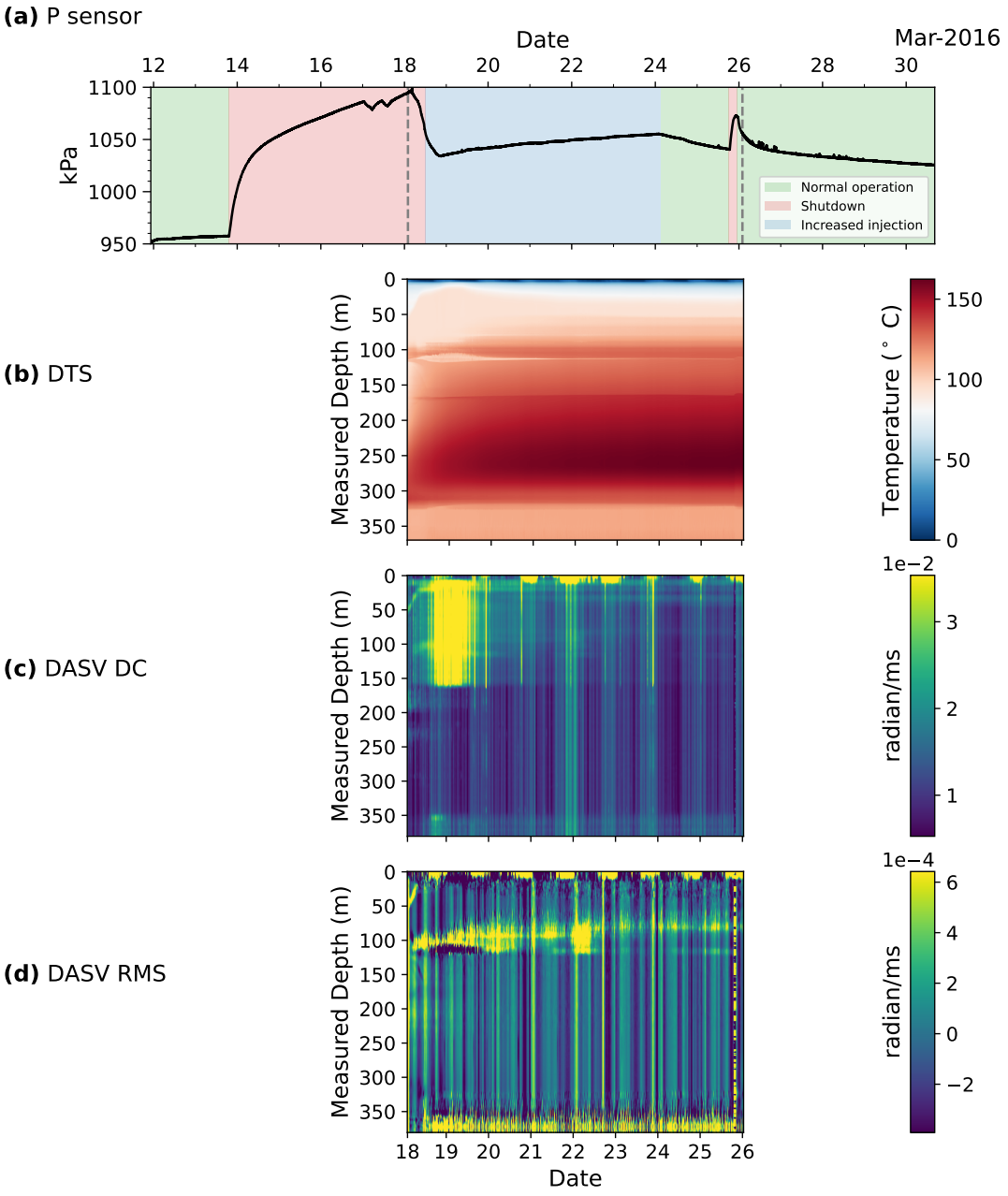

Figure 2. (**a**) Pressure (P) and corresponding field operation stages [30], (**b**) DTS temperature, (**c**) DASV DC amplitude, and (**d**) DASV root-mean-square (RMS) amplitudes of non-filtered observed data aligned in time. The analysis period of this study is 3/18 - 3/25 (eight days; marked by gray dashed lines), when we have all pressure, DTS, and DASV data simultaneously. The DC and RMS amplitudes are calculated with 30 mins time window with 50% overlap.

can examine the wavefields that satisfy different boundary conditions by using different virtual sources.

The deconvolved wavefield D in the frequency domain is [23]

$$D(z, z_a, \omega) = \frac{U_z(\omega)}{U_{z_a}(\omega)} \tag{1}$$

$$\approx \frac{U_z(\omega) U^*_{z_a}(\omega)}{|U_{z_a}|^2 + \varepsilon \langle |U_{z_a}|^2 \rangle} \quad , \tag{2}$$

where z is the depth of each channel, z_a is the depth of the virtual source channel, ω is the angular frequency, and * denotes the complex conjugate. The deconvolution operation in the frequency domain is the division of the data recorded at each depth ($U_z(\omega)$) by the data recorded by the receiver that is used as the virtual source ($U_{z_a}(\omega)$). The instability in Equation 1 comes from the division, and we can stabilize it with a water level $\varepsilon = 0.5\%$ that scales with the average power spectrum ($\langle |U_{z_a}|^2 \rangle$) as shown in Equation 2. Given a selected channel as the virtual source, we calculate the deconvolved wavefield using Equation 2 for the entire 1D array and stack the resulting wavefields over a time span to improve SNR.

We use two sets of these time intervals for calculating the stacked deconvolved wavefield based on empirical testing and Seats *et al.* [31]. The time intervals in this operation include the time window of each trace for one deconvolved wavefield (t_{win}), the time step to slide the time window (t_{step}), and the time span that we stack all the deconvolved wavefields within it and get a final retrieved wavefield (t_{span}). For the purpose of tracking the velocity of the consistent signals (Section 3.2), we use $t_{win} = 1$ min, $t_{step} = 0.5$ min, and $t_{span} = 1$ hr. These short time intervals provide good temporal resolution and SNR since the consistent signals we obtain in the upper part of the borehole are strong. For the purpose of observing the wavefield patterns and treating weak signals (Section 3.1.2 and Appendix A), we use $t_{win} = 30$ min, $t_{step} = 15$ min, and $t_{span} = 3$ hr. These longer time intervals are required for enhancing the SNR in the lower part. Before converting the data to the frequency domain for deconvolution, we demean, detrend, and taper (10% on both sides) the raw data inside t_{win}. For simplicity, we omit the "stacked" term and call the final retrieved wavefield "deconvolved wavefield" for the rest of this paper.

3.1.2. Deconvolved wavefields

The deconvolved wavefields are distinctly different between the upper and lower parts of the borehole. Hence, we analyze them separately. The upper part between 10 - 165 m is dominated by strong reverberating signals that bounces between 10 and 165 m (top panels in Figure 3). Between 165 - 200 m is a transition zone. The lower part is below 200 m - it contains weak direct wave signals and we discuss them in Appendix A (Figure A1).

Here, we focus on the coherent signal in the upper part between 10 - 165 m (Figure 3). The wave complexities and frequency content change over time. We use numerical models to explain the wavefields in Section 3.1.3 and use the separated direct waves to estimate propagation velocity in Section 3.2. We analyze the changes of normal-mode in the frequency domain in Section 3.3. We discuss the extracted transient signals in the lower part in Appendix A since their low SNR does not facilitate precise temporal analysis.

Deconvolution seismic interferometry makes waves interpretable in the upper part of the borehole where the direct waves and the multiples overlap each other. The top panels in Figures 3a - f show the deconvolved wavefields between 0 - 200 m depth that contains strong reverberations. To interpret the deconvolved wavefield, one should know that: (1)

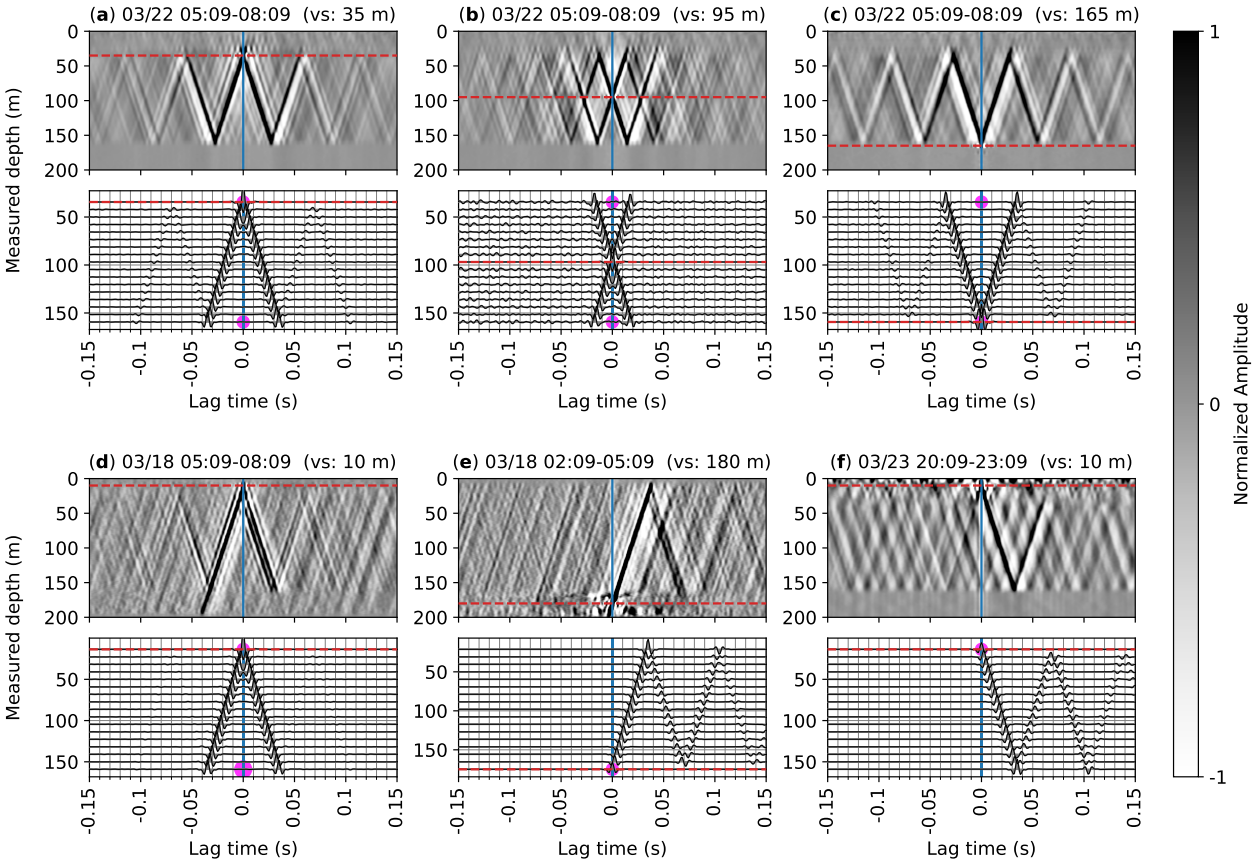

Figure 3. The DASV stacked deconvolved wavefields between measure depth 0 - 200 m (top panels in (**a**) - (**f**)) and the simulated wavefields (bottom panels in (**a**) - (**f**)) using model 1 in Figure 4. The wavefields are plotted for 0.15 s around the zero-lag time (The blue vertical lines). The stack wavefields are calculated using $t_{win} = 30$ min, $t_{step} = 15$ min, and $t_{span} = 3$ hr. The *vs* is the measured depth of the virtual source channel (the red dashed lines). The magenta balls mark the actual source locations. The sizes of the balls are proportional to the amplitude of the actual sources. (**a**) - (**c**) are at the same time but with different virtual sources. These symmetrical wavefields are observed most of the time. (**d**) - (**f**) are cases that show occasional variations. See text for details.

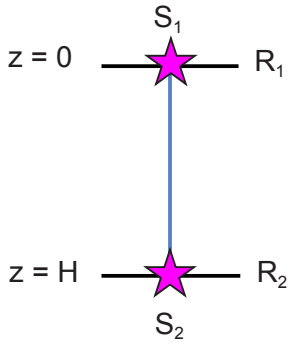

Figure 4. Model 1: A simple 1D string model used to simulate the deconvolved wavefields in Figure 3. A string with a line of receivers on it (blue line) bounded by two reflectors at $z = 0$ (R_1) and $z = H$ (R_2). The two sources are located at $z = 0$ (S_1) and $z = H$ (S_2) (magenta stars).

the waves always propagate toward the positive time direction in field data, (2) the direct wave emits from the virtual source, and (3) the boundary condition at the virtual source is modified as a clamped boundary condition [23]. The wavefields are clearly consisted of up-going and down-going direct waves between 10 m to 165 m. In addition, the direct waves reflect at the boundaries at 10 m and 165 m and cause the multiples reverberating in this depth range. At 165 m, the wavefields have an abrupt change, below which the upper reverberations do not propagate downward. The depth of this abrupt change corresponds to the depth of the advection activities observed in Patterson *et al.* [17] and is interpreted as resulting from a defect on the casing. This depth behaves as a reflector of these waves. In the transition zone between 165 - 200 m, we see strong up-going waves during 3/18 - 3/19 (Figure 3d at around -0.4 s) which means this depth range contains the source for the upper reverberations during this time.

3.1.3. Modeling deconvolved waves

To explain the observed deconvolved wavefields, we use a simple string model following Nakata *et al.* [23] with assumptions that we have a constant velocity in the media and no internal reflectors (Figure 4). This model is based on several noticeable characteristics in the observed wavefields in Figure 3. First, for the majority of the time in the analysis period, the extracted signals are strong in both the causal and acausal times for all the virtual sources in between a depth range (Figures 3a - c). This is not expected if the incoming waves are solely from below or the top of the array [23,29]. Hence, we put two sources - one at the top and one at the bottom of the system (Figure 4). This model can also represent the case when we have sources that are further away from the end points outside of this receiver line [26]. In this case, we consider S_1 and S_2 indicating the incoming waves from the top and the bottom to the system, respectively. Second, direct waves and reverberations are observed from the virtual source and their reflections occur on the top and the bottom boundaries, where the top is the free surface and the bottom is the location of the casing defect. Hence, we put two reflectors, R_1 and R_2, at these two boundaries, respectively.

Mathematical notation of wavefields

We first derive the mathematical notation for the model in Figure 4. Nakata *et al.* [23] expressed the wavefield of a single source as the sum of a power series. Following their results, the wavefields of the two sources in Figure 4 are the superposition of their individual wavefields:

$$U(z,\omega) = \frac{S_1(\omega)(e^{z(ik-\gamma|k|)} + R_2 e^{(2H-z)(ik-\gamma|k|)}) + S_2(\omega)(e^{(H-z)(ik-\gamma|k|)} + R_1 e^{(H+z)(ik-\gamma|k|)})}{1 - R_1 R_2 e^{2H(ik-\gamma|k|)}} \quad (3)$$

where z is depth, ω is the angular frequency, i is the imaginary number, k is the wave number, and H is the length of the structure, γ is the attenuation factor where $\gamma = \frac{1}{2Q}$ [32], S_1 and S_2 denote the spectrum of the two source terms and R_1 and R_2 are the reflection coefficients of the top and bottom reflectors, respectively. In the nominator, $e^{z(ik-\gamma|k|)}$ and $R_2 e^{(2H-z)(ik-\gamma|k|)}$ are the direct wave and the first reflection for S_1, while $e^{(H-z)(ik-\gamma|k|)}$ and $R_1 e^{(H+z)(ik-\gamma|k|)}$ are those for S_2. Their amplitudes are scaled by the attenuation terms that involve γ. The $R_1 R_2 e^{2H(ik-\gamma|k|)}$ term in the denominator is the common ratio in the power series representing higher-order reverberations between two reflectors. With Equations 1 and 3, the deconvolved wavefield using virtual source at z_a ($0 \leq z_a \leq H$) can be written as

$$D(z,z_a,\omega) = \frac{(e^{(z-z_a)(ik-\gamma|k|)} + R_2 e^{(2H-z-z_a)(ik-\gamma|k|)}) + \frac{S_2}{S_1}(e^{(H-z-z_a)(ik-\gamma|k|)} + R_1 e^{(H+z-z_a)(ik-\gamma|k|)})}{(1 + R_2 e^{2(H-z_a)(ik-\gamma|k|)}) + \frac{S_2}{S_1}(e^{(H-2z_a)(ik-\gamma|k|)} + R_1 e^{H(ik-\gamma|k|)})} \tag{4}$$

$$= \frac{\frac{S_1}{S_2}(e^{(z+z_a-H)(ik-\gamma|k|)} + R_2 e^{(H-z+z_a)(ik-\gamma|k|)}) + (e^{(z_a-z)(ik-\gamma|k|)} + R_1 e^{(z_a+z)(ik-\gamma|k|)})}{\frac{S_1}{S_2}(e^{(H+2z_a)(ik-\gamma|k|)} + R_2 e^{H(ik-\gamma|k|)}) + (1 + R_1 e^{2z_a(ik-\gamma|k|)})}. \tag{5}$$

Based on these two equations, we can predict the wavefields of the extreme cases when either S_1 or S_2 is dominant in model 1 (Figure 4). The deconvolved wavefield with two sources approaches the one-source cases when either source is dominant. At these two extrema, symmetry between the causal and acausal time is lost, which is the most obvious in the following two cases. The first case is when $|S_2|/|S_1| \approx 0$ and $z_a = 0$, Equation 4 becomes the infinite series of Equation 9 in Nakata *et al.* [23]. The second case is when $|S_1|/|S_2| \approx 0$ and $z_a = H$, where Equation 5 becomes

$$D(z,H,\omega) = \sum_{n=0}^{\infty}(-1)^n(R_2^n e^{((2n+1)H-z)(ik-\gamma|k|)} + R_2^{n+1} e^{((2n+1)H+z)(ik-\gamma|k|)}). \tag{6}$$

The positive-only ik terms in the exponent in Equation 9 in Nakata *et al.* [23] and Equation 6 suggest the asymmetrical wavefield. To investigate the cases in between these two extrema and whether they can produce the symmetry, we use numerical simulation in below.

Simulating the deconvolved wavefields

We simulate the deconvolved wavefields using Equations 2 and 3 and compare them with observed deconvolved waves qualitatively (Figures 3a - f). After a series of parameter tests shown in Appendix B.1, we set all source terms to be mutually uncorrelated with their cross-correlation coefficient $cc = 0.01$. This choice is because correlated source would generate simultaneous direct waves from the virtual source, as shown in Appendix B.1, which we do not observe in the wavefield. Other parameters used are $Q = 500$, $\omega/k = 4600$ m/s and $\varepsilon = 0.0001\%$, $R_1 = R_2 = 0.9$ for 3a - d, and $R_1 = R_2 = 0.5$ for 3e, f. These choices are based on the low attenuation across depth, apparent velocity of the signal, and reflectivity at the boundaries in the observed data.

The simulations based on the simple 1D string model in Figure 4 explain the symmetry in the observed deconvolved wavefield. The simulated wavefields reproduce the symmetry in Figures 3a - c when the intensities of two sources equal each other ($|S_2|/|S_1| = 1$). This symmetry is observed on most of the time during the analysis period, although the range of H and relative amplitudes might change, which we discuss in below.

The top reflector at 10 m on 3/18 (Figure 3d) is likely the free surface that appears at 10 m due to gauge length. At later days, the top reflector drops to 35 m (Figure 3a), which suggests the boundary is changing. We speculate that this might be related to the observation borehole DAS system and/or the variations of near-surface temperatures, but we need more information to better understand the cause of this change. The amplitude of multiples are smaller in Figure 3d than in 3a. This can be modeled by putting a larger source at the bottom ($|S_2|/|S_1| = 2$) or using a smaller reflection coefficient R_2 to simulate Figure 3d. In Appendices B.2 and B.3, we show the effect of varying relative source intensity and reflection coefficients in this model.

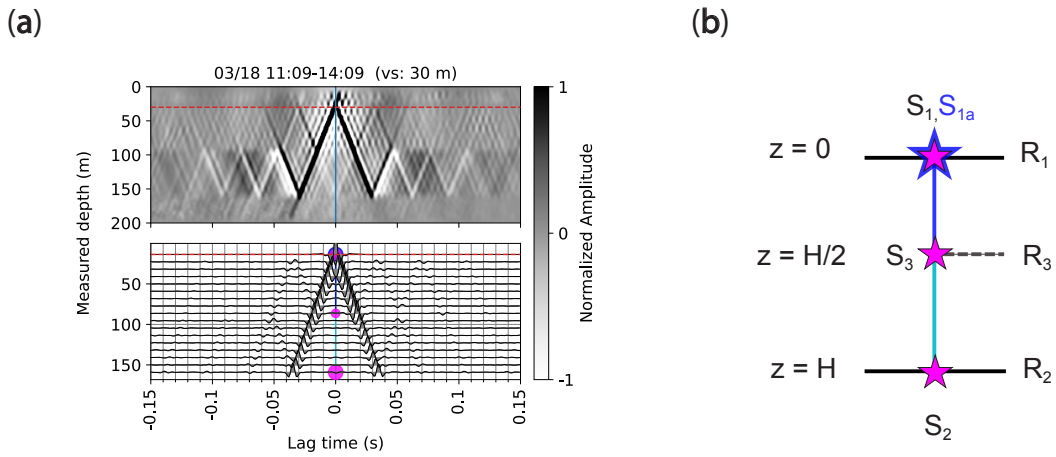

Figure 5. (**a**) The DASV stacked deconvolved wavefield between measure depth 0 - 200 m on 3/18 at noon (top panel) and the simulated deconvolved wavefield (bottom panel) using model 2 in (**b**). (**b**) **Model 2**: A more complicated model than model 1 in Figure 4. In addition to the sources and reflectors in model 1, we add two additional sources and a middle reflector. The first new source S_{1a} is at $z = 0$ (blue star) and propagates only between $z = 0$ - $H/2$ (the dark blue line). The middle reflector at $z = H/2$ has reflection coefficient of R_3 (dashed black line). The other added source is at $z = H/2$ (S_3) and propagates between $z = 0$ - H (both the dark blue and the cyan lines) as the rest of the sources.

The occasional asymmetries observed in the wavefield are explained by changing the relative intensity of the sources and show agreements with the predictions from the analytical solution. In Figure 3e, the strong up-going wave on the causal part is reproduced in the simulation by putting a dominant source at the bottom ($|S_1|/|S_2| \approx 0$). This suggests a strong source from below. We observe this asymmetry on 3/18 - 3/19 for virtual sources in the transition zone between 165 - 200 m. This strong source from below is likely associated with increasing intensity of field operations and the disturbances in the borehole that follows the drastic pressure drop (Figure 2a). In Figure 3f, the strong down-going causal wave is reproduced by putting a dominant source at the top ($|S_2|/|S_1| \approx 0$). This suggests a strong source from the surface. This asymmetry is observed when the vibroseis truck was operating at some of the closest sites to the well (around 100 - 600 m away), which produced large noises sources on the surface. These simulation results with one dominant source agree with predictions from Equations 4, 5.

Some observed deconvolved wavefields suggest a more complicated 1D string model (Figure 5). The observed wavefield in the top panel of Figure 5a shows a reflector at near 90 - 100 m. This more complex wavefield is observed on 3/18 at noon during changing field operation and the drastic pressure drop. To model this wavefields, we consider the influence of the surface outer-casing between 0 - 87 m [19]. The outer-casing is behind the inner-casing with a wider diameter and can be a subsystem that rings by itself. To model this effect, we add an additional source S_{1a} that is co-located with S_1 at $z = 0$ with that generates waves propagating only between $z = 0$ and a reflector R_3 at $z = H/2$ (Figure 5b). We further find that we have to add another source S_3 at $z = H/2$ that generates waves propagating between $z = 0$ - H to better match the relative amplitudes in the wavefield. Without this S_3, we would have a strong down-going wave from 90 to 165 m between -0.02 - 0 s and a strong up-going wave from 165 to to 90 m between 0 - 0.02 s, which we do not see in Figure 5a. The high RMS amplitude near 100 m on 3/18 (Figure 2d) is likely related to this source. Although the cause of this source is not obvious, this is close to the location of changing of the casing diameter [19]. The relative intensities in the final simulated wavefields (bottom panel in Figure 5a) are $S_1 : S_2 : S_3 : S_{1a} = 1 : 2 : 0.7 : 2$.

3.2. Time-lapse changes of wave velocities

To understand the reverberating signal between 10 - 165 m which consistently appears over the entire analysis period and the medium it propagates in, we analyze the wave velocities and their time-lapse changes. For every one hour of ambient-noise data, we can extract coherent traveling waves, and hence we use them to estimate accurate velocities at each hour. We measure the arrival time of up-going waves at each channel by picking the peak of the first arrivals in the deconvolved wavefields. The slopes of the picked arrival times provide the velocities. We focus on channels between 70 - 120 m, where the signal appears consistently over the eight days and shows the highest SNR. We only use the phase parts for our interpretation and do not use the amplitudes, because the amplitudes of the deconvolved waves extracted from ambient noise are complicated to interpret [29]. The modeling shown in Appendix B will help understand the amplitudes. Figure 6 are the measured velocities against measured depth, time, temperature, and pressure. In general, the propagating velocity from first arrival picking is at around 3600 - 5000 m/s, which agrees with the compressional velocity of steel.

Figure 6a shows the velocity estimates across depth across 70 - 120 m. The velocity shows a slight decreasing trend of -6.6 m/s per meter, which reflects the negative temperature-velocity dependency in Figure 6c since the temperature increases with depth at this depth range (Figure 2b). The larger velocity variations (the width of the blue shade) near 72 m and 100 m indicate potential poor coupling between the DAS cable and the casing. However, we note that the larger velocity variation at 100 m can also be related to a change of the casing structure at this depth, which is observed in Figure 5.

Figure 6b is the temporal evolution of velocity across 70 - 120 m over the eight days. In early 3/18, the mean velocity suddenly rises from 4100 to 4700 m/s, then, before late 3/19, it falls back to 4100 m/s and fluctuates between 4100 - 4300 m/s for the remaining time of the eight days. We suspect that the high velocity during 3/18 - 3/19 is associated with the depressurization processes in the borehole due to the initial pressure drop. As suggested by Patterson [18], this depressurization process caused disturbances such as boiling and changes of steam-water interface between 70 - 120 m. During this time, the DAS data also have high DC level at this depth range as shown in Figure 2c. Hence, the high velocity measured during this time is likely related to intense vibration due to the depressurization process.

Figure 6c shows the velocity decreases with increasing temperature with a slope of -17.1 m/s/$^{\circ}C$. The mean dV/dT relation (-17.1 m/s/$^{\circ}$C) is much higher than that measured in the lab for pure steel material using an ultrasonic method (-0.5 m/s/$^{\circ}$C [33,34]). This is because the casing materials are not pure steel [19]. Instead, they are Oil Country Tubular Goods (OCTG) graded alloy steel for higher hardness and corrosion resistance [19]. Thus, we find this non-pure steel has high sensitivity to the temperature.

In Figure 6d, we do not observe obvious correlation between velocity and pressure except for the very low-pressure zones because of the lack of samples at higher pressure.

3.3. Normal-mode analysis

The deconvolved wavefield of a vibrating 1D structure can be written as the summation of normal modes [23,28]. Figure 7 shows the amplitude spectrum of the deconvolved wavefields for a virtual source at 180 m calculated using one minute time window ($t_{win} = 1$ min) and stacked over one hour ($t_{span} = 1$ hr). The normal modes of the signal are clearly decomposed between 10 - 165 m, from 10 to over 200 Hz. The consistent amplitude along depth and frequency suggest the waves propagate in a relatively homogeneous medium (compared to the wave length). The system has closed boundary on both sides (top and

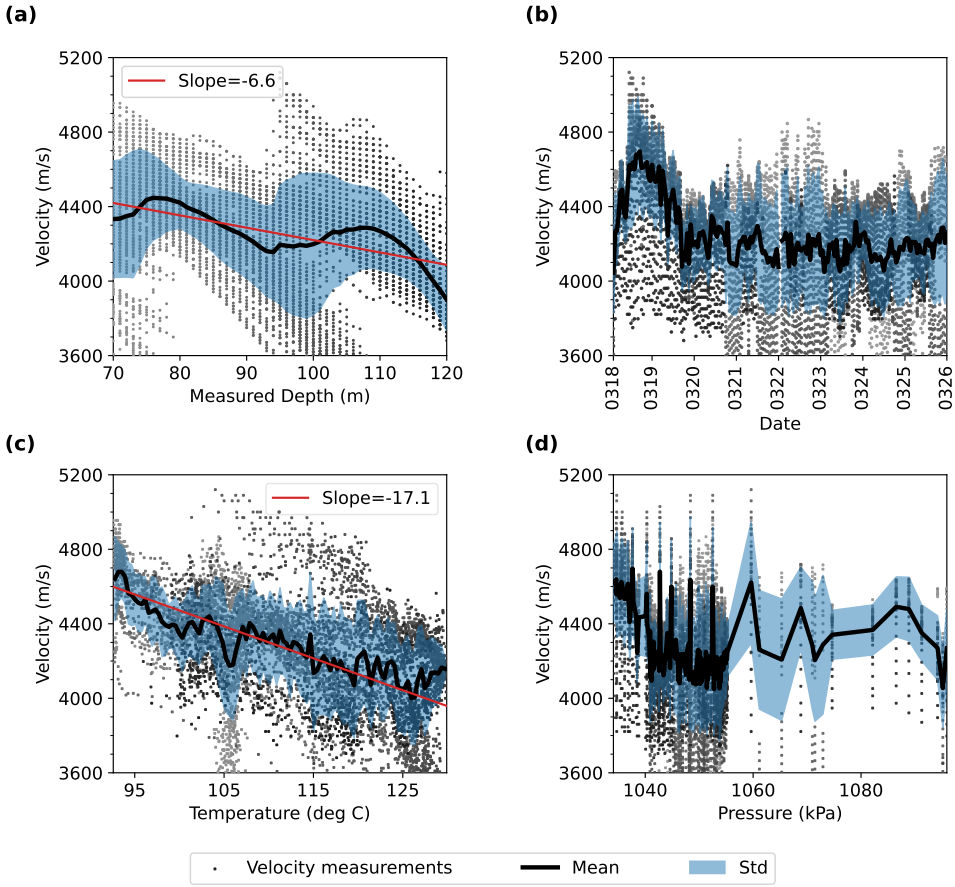

Figure 6. The velocity of the signal between 70 - 120 m versus (**a**) depth, (**b**) time, (**c**) temperature, and (**d**) pressure. The velocities are calculated by measuring the slope of the the first arrivals on the causal side of the hourly stacked deconvolved wavefields. Each black dot is a velocity measurement at one channel, where deeper channels are distinguished by gradually darker colors. The black curves are the mean values. The blue shades mark one standard deviation above and below the mean values. The red lines in (**a**) and (**c**) shows the trend of the linear fit.

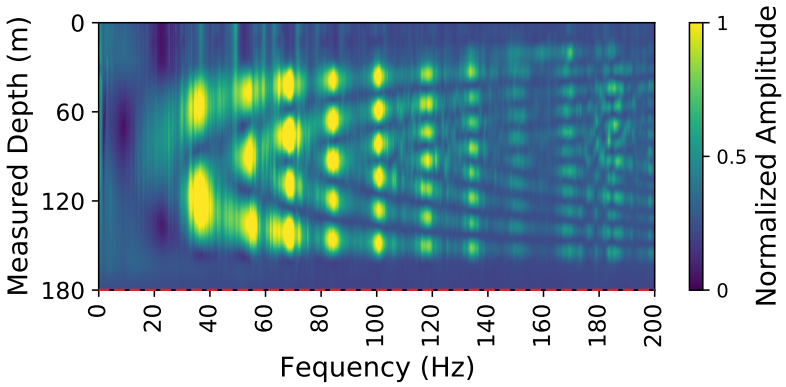

Figure 7. The deconvolved amplitude spectrum of DASV between 0 - 180 m on 3/18 at 6 am ($t_{win} = 1$ min, $t_{span} = 1$ hr). The spectrum shows that the reverberating signal between 10 - 165 m can be decomposed into normal modes. The red dashed line marks the virtual source at 180 m.

bottom; i.e., 10 and 165 m in Figure 7) of the interval. The top boundary is related to the free surface, which behaves as the closed surface for P-waves. For the bottom boundary, because we use the virtual source at 180 m, and the deconvolution modifies the boundary condition (a.k.a. clamped boundary [21]). At the virtual source, the deconvolved wavefields become a delta function (see Equation 1 with $z = z_a$). The delta function indicates that the boundary at the virtual source is closed. The frequency interval between different modes is about 18 Hz and consistent over all modes as expected. The first mode is, based on the shape of the spectrum, at around 20 Hz, but its amplitude is low. The second and higher modes are stronger.

These normal modes are varying, according to previous observation between Figures 3a and 3d where the location of the top reflector changes. This results in changes in the system length (H) and implies potential perturbation of phase velocity (c). Because the phase velocities for a system like model 1 (Figure 4) with closed boundaries are

$$c_m = \frac{2 f_m H}{m} \quad , \tag{7}$$

where m is the mode number, f_m is the mode frequency.

We estimate the velocity changes using Equation 7 focusing on the 2nd (∼38 Hz), the 3rd (∼55 Hz), and the 4th (∼71 Hz) modes, since these three modes are the most significant. We extract f_m by picking the largest peaks in the amplitude spectrum for these three modes in the hourly stacked amplitude spectrum at 6 or 7 am on each day, which is the time that has relatively high SNR. We estimate H by measuring the length of the DAS segment in which the mode is present (i.e., the depth difference between the upper and lower boundaries where the amplitudes reduce to background level).

In Figure 8a, the mode frequencies get slightly higher while the system length gets shorter. The length of the system decreases about 13 m from 140 to 127 m. This corresponds to previous observation that the top boundary of the system in Figure 3d drops in Figure 3a. Figure 8b shows the velocities calculated using Equation 7. The velocities estimated using higher modes are lower, suggesting a negative frequency-velocity dependency, and hence the velocities are dispersive [35]. In general, all of the three modes show similar trends: the velocities increase for the first few days before 3/20, and then, they continuously decrease until the end of the analysis period.

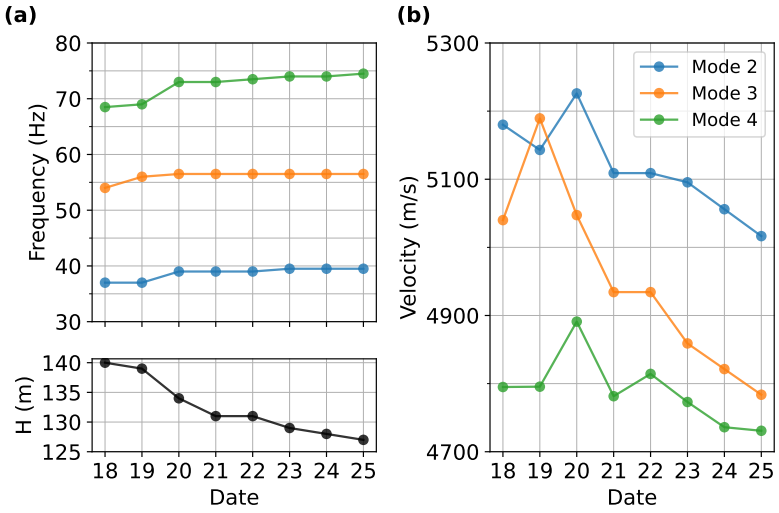

Figure 8. (**a**) The peak frequencies (f_m) and the system length (H) in Equation 7 that are picked for the 2nd, 3rd, and 4th modes in the stacked deconvolved spectrum (e.g., Figure 7). (**b**) The phase velocities of the signals derived from Equation 7.

4. Discussions

4.1. Signals in the upper part between 10 - 165 m

Seismic interferometry by deconvolution allows us to extract direct waves and multiples in the complicated borehole DASV wavefield. By analyzing the extracted waves, we can constrain the location of energy sources and properties of the structure these waves propagates in.

Numerical simulations using simple 1D string models can qualitatively reproduce the direct waves and the multiples in the observed deconvolved wavefields in the upper part between 10 - 165 m (Figures 3, 5). A simple model with two sources and two reflectors in Figure 4 can explain most of the wavefields. Some wavefields exhibit more complexity and require a more sophisticated model with added reflectors and sources 5. Model 2 in Figure 5b suggests an independent wave being trapped between 0 - 90 m, which is likely due to separate vibration of the surface outer-casing. This separate vibration is modeled by adding an independent source (S_{1a}) that generates waves only propagate between $z = 0$ - $H/2$ (the blue star and the blue line in Figure 5b) due to an internal reflector (R_3). We find the potential existence of an internal source (S_3) that helps qualitatively match the relative amplitude above and below the internal reflector. In fact, the actual conditions might be even more complicated and we note that the solutions are not unique. Nevertheless, the models we propose here may be the simplest to explain the observed wavefields. For quantitative analysis of wavefields, we may need to estimate the phase shift at the boundary condition as well as the coherency of wavelets at two sources at different frequencies.

According to mathematical analysis and numerical modeling, the symmetry of the wavefield for a 1D string model in Figure 4 is related to the relative intensity of the noise sources and the reflectivity at the boundaries (Appendices B.2, B.3). According to Nakata and Snieder [29], to have symmetry between the causal and acausal time for all virtual sources in this model, we must have more than one source. We reproduce the symmetry in simulation by having two sources with comparable intensity (Figures 3a - c). If one source is dominant, the wavefield is asymmetrical (Figure B3). In the extreme cases with one source being overwhelmingly dominant, we only have direct wave on the causal time when the virtual source is at the end with the dominant source (Figures 3e, f), which is expected from the mathematical analysis and demonstrated in the numerical simulations.

The main sources in this system include borehole processes, surface operations, and traffic and other anthropogenic noises. These sources contain higher frequencies ($>$ 10 Hz) as observed in the spectrum (Figure 7). The first source is fluid exchange activities between inside and outside of the borehole. In the transition zone between 165 - 200 m, we see strong up-going waves during 3/18 - 3/19 (Figures 3d, e), which means that this depth range contains the source for the reverberations between 10 - 165 m during this time. This source is possibly associated with a potential weak spot on the casing at 165 m, where we likely have fluid advection between the internals of the borehole and the formation [18,19]. In addition, this spot also behaves as a physical reflector to general reverberations because the waves have difficulty to propagate through, although the mechanism is not clear. Second, the high RMS amplitude near 100 m (Figure 2d) is a potential source at least on 3/18 at noon based on model 2, although the exact mechanism is not obvious. We note that the high temperature can induce slow strains on DAS [36] but the induced signals are low-frequency [19]. The third sources are surface operations including site activities and vibroseismic experiments, which were conducted 10 hours a day. The diurnal cycles of the surface DASV RMS amplitude correspond to these activities (Figure 2d). Fourth, the interstate highway on the north-western side of the survey region provides traffic noises as an energy source [37]. The relative intensity of these sources changes over the analysis period, which results in the patterns of the deconvolved signals changes over the time.

The estimated velocity suggest that the extracted waves propagate in the steel casing as P-waves. Because the velocity estimated from the direct waves and normal modes are close to the P-wave velocities in steel rods (5000 - 5250 m/s [38]) for both up-going and down-going waves. The estimated velocity is significantly higher than that in the local formation (V_p=1000 - 2500 m/s [39,40]). These waves are sensitive to the casing, coupling of the casing to the ground, and fluid in the borehole [41]. Hence, the measured velocities and their variations are affected by these conditions. The variation of the measured velocity can potentially help diagnosing locations of poor DAS cable coupling (Figure 6a). However, in this case, these variations are possibly related to change of casing structure since model 2 in Figure 5 suggests more complexities at the depth, which might cause variation of waveforms and thus affect the arrival picking. This casing vibration accelerates and then decelerates during the initial stage of pressure disturbance (Figure 6b), although the trend of the velocity-pressure plot is not obvious due to lack of data coverage (Figure 6d). On the other hand, the velocity appears to be sensitive to the casing material and shows a trend of decreasing velocities with increasing temperature (Figure 6c).

Comparing the velocities estimated by the propagating-wave method (Figures 6) and the normal-mode method (Figure 8), the later yields slightly higher velocities than the former. This is because the normal-mode analysis is done in the lower frequency modes that have higher velocities (Figure 8b) whereas the propagating waves contain all frequencies. The frequency-dependent velocities from the normal-mode analysis are potentially useful to obtain attenuation and structures at different distance from the well. However, in this case, since the coupling between casing and the formation was poor as discussed below, the dispersion relation is less sensitive to the structure. Instead, the negative frequency-velocity relation might be caused by the casing and fluid in the borehole, but we need a further experiment to understand the dispersion of the waves.

The reverberations we extract using deconvolution seismic interferometry can be used to monitor the casing conditions in space and time. If the well-casing is well-bonded to the cement, the reverberation would be damped in a few tens of microseconds [42]. Instead, we observe strong reverberation in the deconvolved wavefield. This reverberation is mainly due to the resonance of the production-well casing, which is possibly caused by losing cement behind the casing above 165 m depth, as suggested by Miller *et al.* [19]. The shaking of the DASV steel cable jacket might also contribute to this signal, but the contribution is neglegible. Because the direct waves disappear when we put the virtual source below

200 m. If the vibration of the cable jacket was a dominant signal, we would expect to see direct waves emitted from virtual sources across the entire cable after deconvolution. The high temperature and thermal gradient can produce low-frequency strain signals on DAS fiber and boost up RMS or DC amplitude [19,36]. These slow strains do not propagate as high frequency waves, and thus, we assume it does not affect the measurement. Detailed responses of DAS measurement to temperature depend on cable design [19,36] and would require lab experiment to calibrate.

4.2. Signals in the lower part below 200 m

The signals we obtain in the lower part of the borehole (below 200 m) are from the energies of different types of waves in the vibroseis experiment (Appendix A). Signals that are from outside of the borehole propagate through the formation and are sensitive to the mechanical properties changes in the formation. However, due to the poor SNR at the lower part of the borehole, it is difficult to analyze the velocity variation with satisfying precision. The poor SNR is due to poor coupling between the cable and casing as the cable slipped during the rewarming [19]. If the coupling were better, the SNR would be improved and we could have signals outside of the vibroseismic experiment times. We can potentially apply the similar time-lapse velocity analysis as in the upper part and infer for changes of mechanical properties in the formation.

5. Conclusion

We demonstrate that deconvolution seismic interferometry can extract time-lapse velocity changes of a system and help us understand the physical sources and boundary of the system. The deconvolved wavefields calculated from Brady distributed acoustic sensing (DAS) borehole data have strong reverberations at the upper part of the borehole (10 - 165 m) due to the resonance of the well-casing. The steel casing is the main medium of the compressional wave propagation for this resonance. The deconvolution method allows us to isolate the pure response of the well-casing from the unknown boundary conditions at depth and use it to monitor the integrity of the well-casing as well as the velocity changes in time. By examining the wavefields at different boundary conditions, we can constrain the seismic energy sources.

We qualitatively explain the extracted wavefield using a simple 1D string model bounded by two reflectors, with sources on both sides that have varying intensities. The keys to explain our observation are the reflection coefficients and the relative source intensity. Based on the numerical modeling of the wavefields, the sources have comparable intensities, but uncorrelated with each other, that create the symmetrical deconvolved wavefields. The absolute values of reflection coefficients at the boundaries should be close to one for long-time reverberations. The dominant energy sources of this reverberation are borehole processes and surface operations in addition to traffic noises. The changes of relative intensity of these sources result in variation of the hourly deconvolved wavefields. Furthermore, the wavefield suggests a occasional separate vibration of the outer surface casing that covers the upper 1/2 part of the ringing range (0 - 87 m), which can be modeled using a more sophisticated model. Despite these variation, we have enough repeatability of the waves to measure accurate velocities.

The velocity analysis suggests that the reverberation along the casing is sensitive to disturbances in the borehole (i.e., well integrity) and perturbation of the alloy steel casing. The wave velocity increases during the initial depressurization processes in the borehole, and in the meantime, it decreases at higher temperature. The higher velocity variation indicates a possible location of poor coupling of the DAS cable; however, it can also be

due to a complication on the casing structure. The normal-mode analysis shows that this velocity is frequency-dependent.

To capture consistent and coherence signal for temporal monitoring the changes in the formation, we need better coupling between the DAS cable and the casing, and between the casing and the formation. In this Brady case, only strong transient sources are captured in the lower part of the borehole (below 200 m), which suggests frictional coupling does not facilitate obtaining consistent coherent energy from the formation in a vertical well under changing temperature and pressure conditions. Whereas the casing resonance in the upper part of the borehole is strong and masks any potential energy from the formation. Nevertheless, we can still obtain information about the integrity of the casing and energy sources by analyzing this resonance for the upper part.

The technique proposed here can be applied to many different borehole DAS applications, for example, diagnosis of the condition of the casing structure which helps prevent gas leakage or water contamination. With better coupling, we can potentially obtain more coherent signals and estimate the properties of the reservoir. Furthermore, we can monitor time-lapse changes with continuous data.

Author Contributions: Conceptualization, H.C. and N.N.; methodology, H.C. and N.N.; software, H.C.; validation, H.C.; formal analysis, H.C.; investigation, H.C.; resources, N.N.; data curation, H.C.; writing—original draft preparation, H.C.; writing—review and editing, N.N.; visualization, H.C.; supervision, N.N.; project administration, N.N.; funding acquisition, N.N. All authors have read and agreed to the published version of the manuscript.

Funding: This study is supported by Japan Oil, Gas and Metals National Corporation and MIT-Indonesia seed funds.

Data Availability Statement: Publicly available data sets were analyzed in this study. This data can be found at the DOE Geothermal Data Registry (GDR) https://gdr.openei.org/

Acknowledgments: We appreciate the advice from Douglas Miller on DAS data processing; this study has benefited from several discussions with him. We also appreciate the suggestions from Michal Chamarczuk. We thank the useful feedback from three anonymous reviewers and Deyan Draganov, which help improve this manuscript significantly. This study is supported by MIT Indonesia Seed Fund. The computing for this project was partly performed at the OU Supercomputing Center for Education & Research (OSCER) at the University of Oklahoma (OU).

Conflicts of Interest: The authors declare no conflict of interest.

Abbreviations

The following abbreviations are used in this manuscript:

DAS	Distributed acoustic sensing
DTS	Distributed temperature sensing
SNR	Signal-to-noise ratio
RMS	Root-mean-square

figuresection

Appendix A. Deconvolved wavefields at the lower part below 200 m

As discussed in Sections 3.1 and 4, the energy of reverberations in the upper part

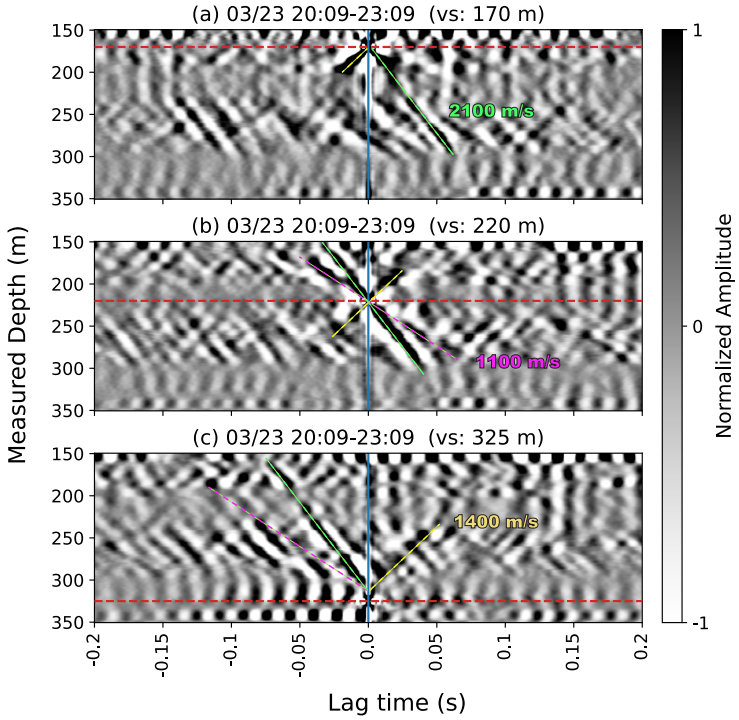

Figure A1. The DASV stacked deconvolved wavefields between measured depth 150 - 350 m during the time where a vibroseis truck was operating at nearby sites (100 - 600 m away). Three sets of signals are obtained using virtual sources at (**a**) 170 m, (**b**) 220 m, and (**c**) 325 m. The red dashed lines indicate the depth of the virtual source (vs). The blue lines are the zero-lag time. The two down-going waves marked by the green and magenta dashed lines have apparent velocity of 2100 m/s and 1100 m/s, respectively. The up-going waves marked by the yellow dashed lines have apparent velocity of 1400 m/s.

between 10 - 165 m becomes very weak at below 165 m. Thus, almost no energy is propagating downward from this depth. We can obtain clear coherent waves only during the times when the vibroseis shots were close to the DASV well. We demonstrate here the extracted waves. These waves have been used, without deconvolution analysis, to identify subsurface structure [20].

We extract clear coherent waves from three-hour stacked deconvolved wavefields between 165 - 300 m during the time when the vibroseis truck was operating closed by (Figure A1). These waves propagate with different velocities. They are not scattering waves as we only obtain these waves in one direction. The poor coupling condition prevents us from getting the scattering energy.

The first two signals travel downward with the apparent velocities of 2100 m/s (green dashed lines) and 1100 m/s (pink dashed line). The actual velocities at this site are V_p = 2300 m/s and V_s = 1200 m/s estimated by Parker *et al.* [39] and Matzel *et al.* [37]. The apparent velocities are close enough to the actual velocities, although they contain some biases due to the incident angle. When the incident angle is nearly vertical (i.e., the wave travels in the axial direction of the cable), the apparent velocities should be close to the actual ones. In our case, because we average wavefields from multiple sources that are distributed at different locations around the well (Figure 1), the bias may be minimized. Note that if we are interested in the time-lapse changes of the velocities, we can still estimate the relative changes using these waves. The V_p/V_s ratio is 1.91 which is consistent for shallow formations in Brady including volcanic sediments, limestone, lacustrine sediments, and geothermal features such as carbonate tufa [43].

The third signal has apparent velocity of 1400 m/s (the yellow dash line) and propagates upward, although it is weak. These waves can be a reflection from nearby faults or bedding planes [20,43], which is the most likely case we can have an up-going wave here. However, we cannot identify the reflection point due to limited amount of good-quality data.

Known changes of the borehole casing likely cause the change in deconvolved waves below 300 m. Notice that using the channel below 300 m as virtual source, the waves still start at 300 m as shown in Figure A1c. Also, the deconvolved waves below 300 m in Figures A1a, b are less coherent and in phase between 300 - 360 m. These feature are like related to the top of the bottom slotted liner at 296 m and the end of production casing at 302 m [19].

Appendix B. Varying model parameters

In Section 3.1.3, we simulate the deconvolved wavefield using model 1 (Figure 4). Here, we show the evolution of the deconvolved wavefield under varying source correlation, relative source intensity, and reflection coefficients. These determine the choice of parameters in our simulations in Figure 3.

Appendix B.1. The effect of source correlation

We vary the correlation coefficient between S_1 and S_2 from 0.01 (uncorrelated) to 0.99 (highly correlated). To generate synthetic data with certain degree of correlation, we first generate random, normalized data time-series and put them in rows to form matrix A. Then, we built a covariance matrix R with the desired correlation coefficient (cc) on the non-diagonals and 1s on the diagonals, and use the Cholesky decomposition to calculate matrix C such that $CC^T = R$. Multiplying A with C gives a new matrix where the cc between each row is as desired.

Figure B2 shows the simulation results when the cc equals 0.01, 0.5, and 0.99. When the two sources are not correlated (Figure B2a), only the virtual source emits waves. When the two sources are correlated (Figures B2b, c), the correlated source seems to emit another set of waves in addition to that from the virtual source; the higher the correlation, the larger the amplitudes of those simultaneous direct waves.

Since we do not observe this simultaneous direct waves in the data, we set $cc = 0.01$ in in simulations in Figure 3.

Appendix B.2. The effect of relative source intensity

We vary the relative intensity of the two source ($|S_1|/|S_2|$) from 0.1, 1, to 10.

The waves emitted from the source exhibit symmetry on both the causal and acausal axes when the two sources have comparable intensities. In Figure B3b, when $|S_1|/|S_2| = 1$, the relative amplitudes on the causal and acausal axes are well-matched regardless of the depth of the virtual source.

The relative amplitude between the causal and acausal waves changes depends on the relative intensity of the sources. In Figure B3a, when $|S_1|/|S_2| = 0.1$, for channels above the virtual source (the red dashed lines), the waves at causal times have larger amplitude, whereas for channels below the virtual source, the waves at acausal times have larger amplitudes. Vice versa, in Figure B3c, the patterns reverse when $|S_1|/|S_2| = 10$.

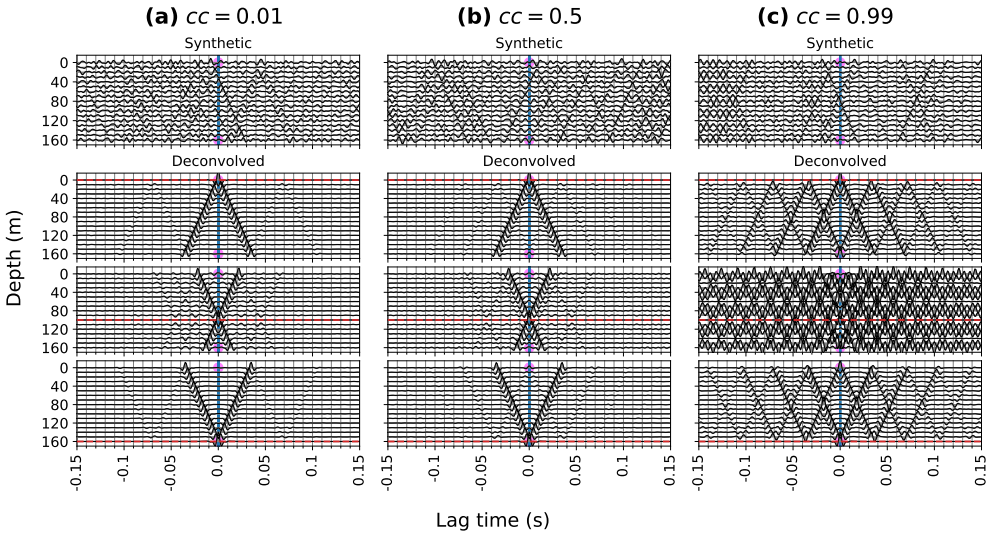

Figure B2. The synthetic and deconvolved wavefields for the two-sources case with varying degree of correlation between them: (**a**) not correlated ($cc = 0.01$), (**b**) partially correlated ($cc = 0.5$), and (**c**) highly correlated ($cc = 0.99$). The actual source locations are shown as the magenta balls in the synthetic wavefields. The virtual sources are shown as the red dashed lines in the deconvolved wavefields. Other parameters are in default values: $|S_1|/|S_2| = 1$, $R_1 = R_2 = 0.5$, $Q = 500$, $\omega/k = 4600$ m/s, and $\varepsilon = 0.0001\%$ that represent the base case.

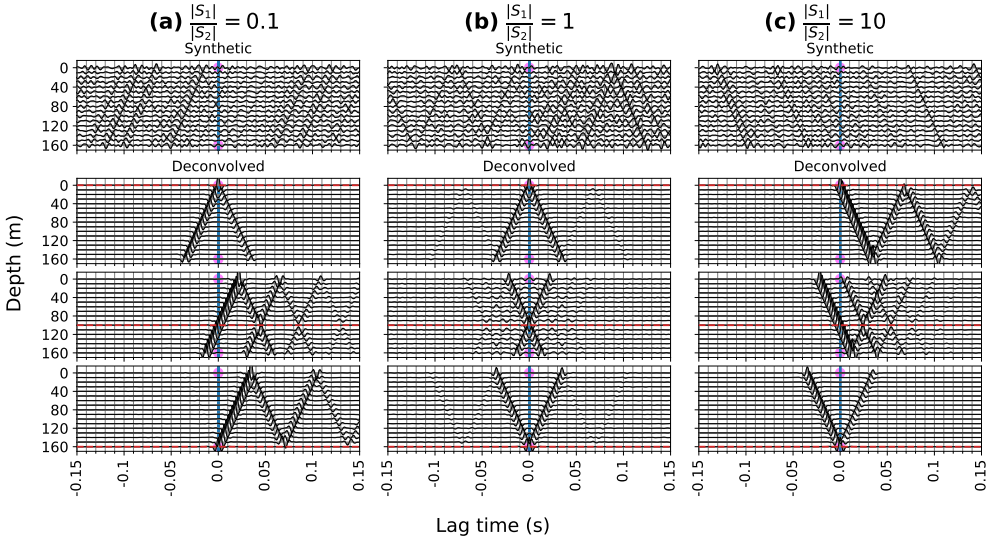

Figure B3. The synthetic and deconvolved wavefields for the two-sources case with varying relative source intensity $|S_1|/|S_2|$: (**a**) strong source from below ($|S_1|/|S_2| = 0.1$), (**b**) sources with equal amplitudes ($|S_1|/|S_2| = 1$), and (**c**) strong source from above ($|S_1|/|S_2| = 10$). Other parameters are in default values: $R_1 = R_2 = 0.5$, $cc = 0.01$, $Q = 500$, $\omega/k = 4600$ m/s, and $\varepsilon = 0.0001\%$ that represent the base case.

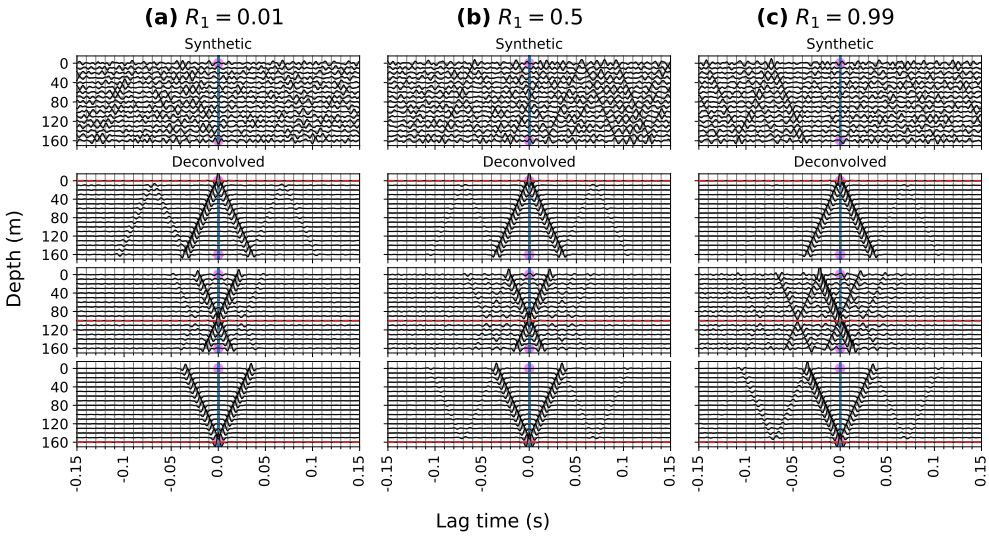

Figure B4. The synthetic and deconvolved wavefields for the two-sources case with varying reflection coefficient of the top reflector R_1: (**a**) low reflectivity ($R_1 = 0.01$), (**b**) intermediate reflectivity ($R_1 = 0.5$), and (**c**) high reflectivity ($R_1 = 0.99$). Other parameters are in default values: $|S_2|/|S_1| = 1$, $R_2 = 0.5$, $cc = 0.01$, $Q = 500$, $\omega/k = 4600$ m/s, and $\varepsilon = 0.0001\%$ that represent the base case.

Hence, to obtain similar results as for the field data, where we have almost equivalent energy in the causal and acausal parts, we need to have two sources with about identical energy. Because the energy balance between the causal and acausal parts varies over the time (Figure 3), the location and/or intensity of the sources may change over time. When one of the sources is dominant (Figures B3a, c and Figures 3e, f), the deconvolved wavefields approach the one-source cases, as predicted by Equations 4, 5.

The time shift between multiples is largest when the virtual source corresponds to the dominant real source. If we move the virtual source away from the dominant source, the multiples start to overlap; the farther away the virtual source is from the real source, the smaller the apparent time shift between the multiples.

Appendix B.3. The effect of reflection coefficients

Figure B4 shows the wavefields with variety of R_1 from 0.01, 0.5, to 0.99. When R_1 gets larger, for channels above the virtual source, the amplitudes of the acausal waves are enhanced; whereas for channels below the virtual source, the amplitudes of the causal waves are enhanced. This phenomenon of a larger R_1 is the opposite of the effect of larger S_1. Hence, the relative amplitudes between the causal and acausal axes can be affected by both the relative source intensity and the reflection coefficients. We need comparable R_1 and R_2 to have symmetry.

We use $R_1 = R_2 = 0.9$ to simulate the wavefield in Figures 3a - d and $R_1 = R_2 = 0.5$ for Figures 3e, f.

References

1. Johannessen, K.; Drakeley, B.K.; Farhadiroushan, M.; others. Distributed Acoustic Sensing-a new way of listening to your well/reservoir. SPE Intelligent Energy International. Society of Petroleum Engineers, 2012.

2. Finfer, D.C.; Mahue, V.; Shatalin, S.; Parker, T.; Farhadiroushan, M.; others. Borehole Flow Monitoring using a Non-intrusive Passive Distributed Acoustic Sensing (DAS). SPE Annual Technical Conference and Exhibition. Society of Petroleum Engineers, 2014.
3. Naldrett, G.; Cerrahoglu, C.; Mahue, V.; others. Production monitoring using next-generation distributed sensing systems. *Petrophysics* **2018**, *59*, 496–510.
4. Dickenson, P. ESP Monitoring using Heterodyne Distributed Vibration Sensor (hDVS). European Artificial Lift Forum, 2014.
5. Mateeva, A.; Lopez, J.; Potters, H.; Mestayer, J.; Cox, B.; Kiyashchenko, D.; Wills, P.; Grandi, S.; Hornman, K.; Kuvshinov, B.; others. Distributed acoustic sensing for reservoir monitoring with vertical seismic profiling. *Geophysical Prospecting* **2014**, *62*, 679–692.
6. Daley, T.; Miller, D.; Dodds, K.; Cook, P.; Freifeld, B. Field testing of modular borehole monitoring with simultaneous distributed acoustic sensing and geophone vertical seismic profiles at Citronelle, Alabama. *Geophysical Prospecting* **2016**, *64*, 1318–1334.
7. Byerley, G.; Monk, D.; Aaron, P.; Yates, M. Time-lapse seismic monitoring of individual hydraulic frac stages using a downhole DAS array. *The Leading Edge* **2018**, *37*, 802–810.
8. Correa, J.; Pevzner, R.; Bona, A.; Tertyshnikov, K.; Freifeld, B.; Robertson, M.; Daley, T. 3D vertical seismic profile acquired with distributed acoustic sensing on tubing installation: A case study from the CO2CRC Otway Project. *Interpretation* **2019**, *7*, SA11–SA19.
9. Webster, P.; Wall, J.; Perkins, C.; Molenaar, M. Micro-seismic detection using distributed acoustic sensing. In *SEG Technical Program Expanded Abstracts 2013*; Society of Exploration Geophysicists, 2013; pp. 2459–2463.
10. Ghahfarokhi, P.K.; Wilson, T.H.; Carr, T.R.; Kumar, A.; Hammack, R.; Di, H. Integrating distributed acoustic sensing, borehole 3C geophone array, and surface seismic array data to identify long-period long-duration seismic events during stimulation of a Marcellus Shale gas reservoir. *Interpretation* **2019**, *7*, SA1–SA10.
11. Hartog, A.H. *An introduction to distributed optical fibre sensors*; CRC press, 2017.
12. Bruno, M.S.; Lao, K.; Oliver, N.; Becker, M. Use of Fiber Optic Distributed Acoustic Sensing for Measuring Hydraulic Connectivity for Geothermal Applications. Technical report, GeoMechanics Technologies, Monrovia, CA (United States), 2018.
13. Munn, J.D.; Coleman, T.I.; Parker, B.L.; Mondanos, M.J.; Chalari, A. Novel cable coupling technique for improved shallow distributed acoustic sensor VSPs. *Journal of Applied Geophysics* **2017**, *138*, 72–79.
14. Zhan, Z. Distributed acoustic sensing turns fiber-optic cables into sensitive seismic antennas. *Seismological Research Letters* **2020**, *91*, 1–15.
15. Feigl, K.L.; Team, P. Overview and preliminary results from the PoroTomo project at Brady Hot Springs, Nevada: Poroelastic tomography by adjoint inverse modeling of data from seismology, geodesy, and hydrology. 42nd Workshop on Geothermal Reservoir Engineering. Stanford University Stanford, CA, 2017, pp. 1–15.
16. Feigl, K.L.; Parker, L.M. PoroTomo Final Technical Report: Poroelastic Tomography by Adjoint Inverse Modeling of Data from Seismology, Geodesy, and Hydrology. Technical report, Univ. of Wisconsin, Madison, WI (United States), 2019.
17. Patterson, J.R.; Cardiff, M.; Coleman, T.; Wang, H.; Feigl, K.L.; Akerley, J.; Spielman, P. Geothermal reservoir characterization using distributed temperature sensing at Brady Geothermal Field, Nevada. *The Leading Edge* **2017**, *36*, 1024a1–1024a7.
18. Patterson, J.R. Understanding constraints on geothermal sustainability through reservoir characterization at Brady Geothermal Field, Nevada. PhD thesis, University of Wisconsin–Madison, 2018.
19. Miller, D.E.; Coleman, T.; Zeng, X.; Patterson, J.R.; Reinisch, E.C.; Cardiff, M.A.; Wang, H.F.; Fratta, D.; Trainor-Guitton, W.; Thurber, C.H. DAS and DTS at Brady Hot Springs: observations about coupling and coupled interpretations. Proceedings of the 43rd Workshop on Geothermal Reservoir Engineering, Stanford, CA, USA, 2018, pp. 12–14.
20. Trainor-Guitton, W.; Guitton, A.; Jreij, S.; Powers, H.; Sullivan, B. 3D Imaging of Geothermal Faults from a Vertical DAS Fiber at Brady Hot Spring, NV USA. *Energies* **2019**, *12*, 1401.
21. Snieder, R.; Sheiman, J.; Calvert, R. Equivalence of the virtual-source method and wave-field deconvolution in seismic interferometry. *Physical Review E* **2006**, *73*, 066620.
22. Snieder, R.; Miyazawa, M.; Slob, E.; Vasconcelos, I.; Wapenaar, K. A comparison of strategies for seismic interferometry. *Surveys in Geophysics* **2009**, *30*, 503–523.
23. Nakata, N.; Snieder, R.; Kuroda, S.; Ito, S.; Aizawa, T.; Kunimi, T. Monitoring a building using deconvolution interferometry. I: Earthquake-data analysis. *Bulletin of the Seismological Society of America* **2013**, *103*, 1662–1678.
24. Sawazaki, K.; Sato, H.; Nakahara, H.; Nishimura, T. Time-lapse changes of seismic velocity in the shallow ground caused by strong ground motion shock of the 2000 Western-Tottori earthquake, Japan, as revealed from coda deconvolution analysis. *Bulletin of the Seismological Society of America* **2009**, *99*, 352–366.
25. Yamada, M.; Mori, J.; Ohmi, S. Temporal changes of subsurface velocities during strong shaking as seen from seismic interferometry. *Journal of Geophysical Research: Solid Earth* **2010**, *115*.
26. Nakata, N.; Snieder, R. Estimating near-surface shear wave velocities in Japan by applying seismic interferometry to KiK-net data. *Journal of Geophysical Research: Solid Earth* **2012**, *117*.
27. Bonilla, L.F.; Guéguen, P.; Ben-Zion, Y. Monitoring coseismic temporal changes of shallow material during strong ground motion with interferometry and autocorrelation. *Bulletin of the Seismological Society of America* **2019**, *109*, 187–198.
28. Snieder, R.; Safak, E. Extracting the building response using seismic interferometry: Theory and application to the Millikan Library in Pasadena, California. *Bulletin of the Seismological Society of America* **2006**, *96*, 586–598.

29. Nakata, N.; Snieder, R. Monitoring a building using deconvolution interferometry. II: Ambient-vibration analysis. *Bulletin of the Seismological Society of America* **2014**, *104*, 204–213.
30. Cardiff, M.; Lim, D.D.; Patterson, J.R.; Akerley, J.; Spielman, P.; Lopeman, J.; Walsh, P.; Singh, A.; Foxall, W.; Wang, H.F.; others. Geothermal production and reduced seismicity: Correlation and proposed mechanism. *Earth and Planetary Science Letters* **2018**, *482*, 470–477.
31. Seats, K.J.; Lawrence, J.F.; Prieto, G.A. Improved ambient noise correlation functions using Welch's method. *Geophysical Journal International* **2012**, *188*, 513–523.
32. Aki, K.; Richards, P.G. *Quantitative seismology*; University Science Books, 2002.
33. Mott, G. Temperature dependence of ultrasonic parameters. *Review of progress in quantitative nondestructive evaluation.* **1984**, *3*, 1137–1148.
34. Droney, B.; Mauer, F.; Norton, S.; Wadley, H.N. Ultrasonic Sensors to Measure Internal Temperature Distribution. In *Review of Progress in Quantitative Nondestructive Evaluation*; Springer-Verlag US, 1986; Vol. 5A, chapter Chapter 3: Sensors and Signal Processing, pp. 643–650.
35. Stein, S.; Wysession, M. *An introduction to seismology, earthquakes, and Earth structure*; Blackwell Publishing, 2003; pp. 93–101.
36. Bakku, S.K. Fracture characterization from seismic measurements in a borehole. PhD thesis, Massachusetts Institute of Technology, 2015.
37. Matzel, E.; Zeng, X.; Thurber, C.; Morency, C.; Feigl, K.; others. Using Virtual Earthquakes to Characterize the Material Properties of the Brady Hot Springs, Nevada. *Geothermal Resources Council* **2017**.
38. Haynes, W.M. *CRC handbook of chemistry and physics*; CRC press, 2014.
39. Parker, L.; Thurber, C.; Zeng, X.; Li, P.; Lord, N.; Fratta, D.; Wang, H.; Robertson, M.; Thomas, A.; Karplus, M.; others. Active-source seismic tomography at the Brady Geothermal Field, Nevada, with dense nodal and fiber-optic seismic arrays. *Seismological Research Letters* **2018**, *89*, 1629–1640.
40. Thurber, C.H.; Parker, L.; Li, P.; Fratta, D.; Zeng, X.; Feigl, K.L.; Ak, E.; Lord, N. Active-Source Seismic Tomography at Bradys Geothermal Field, Nevada, with Dense Nodal and Fiber-Optic Seismic Arrays. AGU Fall Meeting Abstracts, 2017, Vol. 2017, pp. S32A–04.
41. Rama Rao, V.; Vandiver, J. Acoustics of fluid-filled boreholes with pipe: Guided propagation and radiation. *The Journal of the Acoustical Society of America* **1999**, *105*, 3057–3066.
42. Ellis, D.V.; Singer, J.M. *Well logging for earth scientists*; Vol. 692, Springer, 2007.
43. Siler, D.L.; Faulds, J.E. Three-dimensional geothermal fairway mapping: examples from the western Great Basin, USA. Technical report, Geothermal Resources Council, Davis, CA (United States), 2013.